Journal of Advanced Joining Processes 7 (2023) 100137

Contents lists available at ScienceDirect

Journal of Advanced Joining Processes

journal homepage: www.sciencedirect.com/journal/journal-of-advanced-joining-processes

Electrografting of BTSE: Zn films for advanced steel-aluminum joining by plastic deformation

B. Duderija [a], A. González-Orive [a,b,*], H.C. Schmidt [c], J.C. Calderón [a,b], I. Hordych [d], H.J. Maier [d], W. Homberg [e], G. Grundmeier [a,*]

[a] Technical and Macromolecular Chemistry, Universität Paderborn, Warburger Str. 100, 33098, Paderborn, Germany
[b] Department of Chemistry, Materials and Nanotechnology Institute, University of La Laguna, Avda. Astrofísico Francisco Sánchez s/n, 38206, San Cristóbal de La Laguna, Spain
[c] Euscher GmbH & Co. KG, Johanneswerkstr. 22, 33611, Bielefeld
[d] Institut für Werkstoffkunde (Materials Science), Leibniz Universität Hannover, An der Universität 2, 30823, Garbsen, Germany
[e] Forming and Machining Technology, Universität Paderborn, Warburger Str. 100, 33098, Paderborn, Germany

ARTICLE INFO

Keywords:
Electrografting
BTSE
Zinc doping
Corrosion protection
Adhesion-promoting layer
Cold-pressure welding (CPW)
Bond strength

ABSTRACT

This article presents the application of an adhesion promoting highly crosslinked ultrathin organic-inorganic hybrid layer applied to steel which promotes the subsequent joining process based on plastic deformation. The tensile shear results show that a significant increase of the bond strength between low-alloy steel (DC04) and aluminum (AW1050A H111), upon cold-pressure welding (CPW), could be achieved. Electrografting of an ultrathin film of 1,2-bis(triethoxysilyl)ethane (BTSE) films on the steel surface was done from ethanolic solutions containing zinc ions. Based on surface spectroscopic analysis it is shown that silanol moieties present in the organosilane deposits can form stable chemical bonds with both the iron oxide covered steel and the aluminum oxide covered aluminum alloy. The successful modification of metal oxide surfaces with BTSE has been demonstrated via SEM-EDX, AFM, PM-IRRAS, and XPS measurements. In addition, electrochemical analysis of the BTSE:Zn films showed that the films lead to very good corrosion properties even at low thicknesses.

Introduction

Joining metals by plastic deformation allows manufacturing metallic welds of high quality (Mori and Abe, 2018; Meschut et al., 2022). It is based on the solid-state welding process known as 'cold welding',which establishes a weld (bond) between two metals without heat, solder or cast. Therefore, no intersolubility is necessary. This offers great opportunities if the deformation process is capable of creating the necessary welding conditions. In most cases, this requires the application of a high pressure, in order to deform both metals and extrude virgin material through cracks in the cover layers (Mori et al., 2013; Bay, 1979, 1983; Bay et al., 1985; Schmidt, 2018). These welding processes are called cold-pressure welding (CPW) (Schmidt et al., 2016). The removal of organic and inorganic contaminants, together with the removal or reduction of the thickness of the native oxide layer, has been shown to significantly increase the bonding between metallic phases in cold pressure welding processes (Li et al., 2008). While the first task can be done just by a simple solvent cleaning step, the latter can be achieved by brushing, chemical, and, interestingly, electrochemical methods. In this regard, Ebbert et al. showed that after electrochemical reduction of the native oxide layer present on copper specimens, which included a remarkable enhancement of the surface roughness, higher values of weld strength were obtained (Ebbert et al., 2014). Similarly, electrochemical cycling of steel surfaces improved the bond strength between steel and aluminum upon welding (Schmidt et al., 2019).

The surface modification of metals and metallic oxides with organic/inorganic molecules has attracted considerable attention over the years since it offers the possibility to functionalize the surface, thus altering their native interfacial properties. In this context, molecules carrying different functional groups are well known to form self-assembled monolayers on a vast variety of metallic oxide surfaces (Pujari et al., 2014). In particular, phosphonates, carboxylates, silanol, and amine groups are reported to bind strongly to, for instance, copper, steel, aluminum oxide and zinc oxide.

As published elsewhere (Toledano and Mandler, 2010; Goux et al., 2009; Collinson and Howells, 2000; Ikjoo et al., 2013), organosilanes are

* Corresponding authors.
E-mail addresses: agorive@ull.edu.es (A. González-Orive), guido.grundmeier@uni-paderborn.de (G. Grundmeier).

https://doi.org/10.1016/j.jajp.2022.100137

Available online 24 November 2022

known to form thin films covalently attached to hydroxyl-rich metallic oxide surfaces. Indeed, the grafting of alkoxysilanes has been carried out on different substrates such as gold, glass, aluminum, iron oxide, etc. In the seminal work by Huser et al. the authors demonstrated the formation of thin films based on several organosilanes on a very low reactive stainless steel 316L surface (Huser et al., 2013). Accordingly, Hoppe et al showed in a recent paper that a self-assembled multilayer of MPTS chemisorbed to an oxide-free copper surface by means of Cu-S bonds was able to increase significantly the shear strength in copper/ aluminum welded joints (Hoppe et al., 2016). This approach required a second step consisting of heating the as-prepared welded samples at 200 °C to promote the condensation of silanols groups, present in the MPTS layer, with the hydroxyl-rich aluminum oxo-hydroxide surface (Gandhi et al., 2007). Interestingly, the deposition and chemisorption of organosilane-based films can also be addressed by electrochemical methods as stated by Sayen and Walcarius (2003), Luna-Vera et al. (2012) and Shacham et al. (1999). In recent contributions by Hu and co-workers, an organosilane/Zn-based composite was electrochemically deposited on steel to increase the corrosion protection (Wu et al., 2012; Liu et al., 2016). As stated by Walcarius (Goux et al., 2009), a first step corresponding to the hydrolysis of siloxane groups to silanols in mild-acidic media, followed by a second step involving the condensation of the as-obtained silanol groups catalyzed by the induced potential-controlled rise in the pH in the vicinity of the electrode, and is required to complete the chemisorption process.

Joining steel to aluminum laminates constitutes a very interesting approach for the design of tailored lightweight materials (Atabaki et al., 2014). In this context, the effect of surface conditioning and thermal annealing on the weld strength registered for the joining between galvanized steel and aluminum specimens by CPW has been reported recently (Hoppe et al., 2016). Modifying metal interfaces with bifunctional molecules that could bind to both dissimilar metal oxide surfaces might have a noticeable impact on the bond strength of the welded specimens (Hoppe et al., 2016). In this sense, 1,2-bis(triethoxysilyl) ethane (BTSE) has been used in dental amalgams and as a primer for epoxy bonding (Jiang et al., 2015; 2015; Jin et al., 2019; Matinlinna et al., 2006). Some preliminary studies showed promising results for the use of BTSE as an adhesion-promoting layer (Schmidt et al., 2019; 2018).

In the present study, electrografting of Zn doped BTSE nanocomposite thin films that enhance the interfacial adhesion between steel and aluminum specimens in CPW processing is shown. A modification of low-alloy DC04 steel substrates with BTSE or a BTSE-Zn composite thin film by cathodic polarization was carried out, before being welded to aluminum sheets (AW1050A H111) by means of CPW. Welded specimens were subsequently submitted to a thermal treatment at 200 °C in order to promote cross-linking within the Si-O-Si crosslinked matrix and condensation of silanol groups present in the latter to both oxide-covered surfaces. Enhanced corrosion protection and bond strengths for the as-formed joinings were obtained.

Experimental

Materials and chemicals

In the initial step, the low-alloy DC04 steel and AW1050A H111 aluminum plates (purchased from Thyssenkrupp and Alumeco Deutschland GmbH, respectively) were solvent cleaned, i.e. ultrasonicated for 15 min. in pure tetrahydrofuran, isopropanol, and ethanol. 1,2-bis(triethoxysilyl)ethane (96 %), BTSE, $Zn(NO_3)_2{\cdot}6H_2O$, $NaNO_3$ (99 %), tetrabutylammonium tetrafluoroborate (Bu_4NBF_4), and anhydrous CH_3CN (ACN) were acquired from Sigma-Aldrich.

Surface pre-conditioning and electrochemical modification of the substrate surfaces

For the optimization of the welding process by plastic deformation, the removal of organic and inorganic contaminants, and the reduction of the native oxide layer at the specimen surfaces is crucial to promote metal-to-metal binding (Li et al., 2008). Consequently, AW1050A H111 substrates were dipped into a 10 % NaOH aqueous solution at 50 °C for $t = 2$ min. in order to remove the native oxide layer (Hoppe et al., 2016). Hoppe et al. showed via of XPS measurements a significant decrease in the thickness of the aluminum oxide layer from 3.8 to 2.1 nm after the surface pickling treatment (Hoppe et al., 2016). Next, the pickled aluminum samples were rinsed thoroughly in Milli-Q water and dried under N_2 flow. The DC04 steel samples were ground with SiC paper (grit size 120, WS Flex, Hermes) for 2 min. The samples were then cleaned with Milli-Q water and ethanol, dried under nitrogen flow and dipped into a 25 $g{\cdot}L^{-1}$ NaOH (99 % from Sigma-Aldrich) aqueous solution at 55°C for 1 min, in order to ensure that a hydroxyl-rich steel surface can be obtained (Gharagozlou et al., 2016; Parhizkar et al., 2018; 2017). FE-SEM and AFM images registered for DC04 and AW1050A H111 before and after every single surface treatment step are displayed in Figs. S1 and S2, and S3 and S4, respectively, in the supporting information (SI). The latter confirms the successful increase in the roughness on the nano and microscale, which is accompanied by a decrease in the oxide layer thickness. These are key effects needed to promote metal-to-metal binding in plastic-deformation-based welding processes (Li et al., 2008; Hoppe et al., 2016).

A three-electrode glass cell setup was used to carry out the electrochemical measurements. The DC04 plates (2×7 cm^2) were the working electrodes, a gold coil was used as the counter electrode, and a commercial Ag/ AgCl (3M KCl, Radiometer analytical) was the reference electrode. A potentiostat Reference 600^{TM} (Gamry Instruments) was used to carry out chronoamperometry and cyclic voltammetry experiences.

Electrografting was performed according to the process described by Shacham et al. (1999). The authors proposed in this innovative contribution a modification to the one pot sol-gel synthesis for the surface modification of ITO with alkoxysilane-sol-gel-based multilayers (Shacham et al., 1999). Briefly, this new two-step methodology consisted of separating the hydrolysis step for the conversion of siloxane to silanol groups from the second step, i.e. polycondensation, which was carried out in an electrochemical cell by applying a sufficiently negative cathodic potential with the subsequent increase of the pH in the close vicinity of the electrode surface. The latter is expected to further promote the polycondensation of the as-formed silanol moieties and their subsequent covalent grafting to the hydroxyl-rich steel surface. As previously stated, this local increase in the pH at negative applied potentials is attributed to the arising of OH^- ions as a consequence of the overlapping and/or successive electroreduction of H^+ ions (hydrogen evolution reaction, *HER*), O_2, and NO_3^- ions.

In our present study, the organosilane sol-gel precursor was prepared by adding BTSE to a 75/25 (v/v) ethanol/ Milli-Q water solution to achieve a final BTSE concentration of 2.5% (w/w). The pH was lowered to 4.5 by adding drops of a 0.1 M CH_3COOH (65 % Sigma-Aldrich) aqueous solution. The as-prepared mixture was stirred for 48 h at 25 °C in a closed beaker to achieve hydrolysis. Then, only $NaNO_3$ or a mixture of the latter and $Zn(NO_3)_2{\cdot}6H_2O$ (50 mM), but maintaining a final constant concentration of NO_3^- ions of 0.2 M, were added into the solution in order to promote the condensation reaction. Samples modified by adding only $NaNO_3$ as electrolyte in the BTSE organosilane-solution are referred to as BTSE, whereas the samples modified by using the $Zn(NO_3)_2{\cdot}6H_2O$-containing electrolyte are labelled as BTSE: Zn.

For the preparation of the organosilane-based thin films, the solvent cleaned and 120 grit size ground DC04 samples were immersed into the previously hydrolyzed BTSE sol-gel precursor solution. A cathodic

potential of -1.2 V (vs. Ag/ AgCl) was applied for growing immersion times. Thereafter, the organosilane-modified steel samples were thoroughly rinsed in ethanol and Milli-Q water, dried under nitrogen flow, cured in air for 15 min at 100 °C, and stored in vacuum.

Joining process and tensile shear testing

Modified specimens from AW1050A H111 aluminum and DC04 steel (both with a size of 100 mm x 20 mm x 1 mm) were welded using an incremental roll-shaped tool with an overlapping length of 40 mm according to the procedure thoroughly discussed in references (Schmidt et al., 2019; Hoppe et al., 2016; Schmidt et al., 2018). Briefly, the two specimens were pressure welded at the center of the overlapped section for a thickness reduction of 75 %, as illustrated in Fig. 1. The aluminum blank was positioned on top of the steel blank, so that the rolling tool was in contact with the aluminum specimen.

After the welding process and with the aim to promote the condensation of silanol to hydroxyl groups at the aluminum oxide surface, AW1050A H111-BTSE-DC04 harnessed joinings were heated to 200° C or 400 °C for $t = 1$ h in a N_2 atmosphere (Hoppe et al., 2016; Gandhi et al., 2007).

The shear forces were obtained by using a Zwick Z100 universal tensile testing machine which incorporates an automatic mechanical extensometer allowing measurements of longitudinal and transverse elongation. The pre-loading force was 73 N, which was progressively increased at 5 N/s until failure. The here presented shear strength results have been averaged from at least 5 welded specimens for each surface combination.

Atomic force microscopy (AFM)

AFM imaging was carried out using a MFP-3D-SA (Asylum Research) equipped with an anti-vibration table and an acoustic enclosure in intermittent contact mode operating in ambient air conditions at a scan rate of 0.5-1.2 Hz. To this end, HQ:NSC15/ AlBS (325 kHz, and 40 $N{\cdot}m^{-1}$, nominal radius of 8 nm) and HQ:NSC18/ AlBS tips (75 kHz, and 2.8 $N{\cdot}m^{-1}$, nominal radius of 8 nm), purchased from Mikromasch, were used. RMS roughness measurements were obtained from the average of the roughnesses collected from three different 5.0 × 5.0 μm^2 areas present in three equally prepared samples.

Field-emission scanning electron microscopy (FE-SEM)

SEM images of the bare substrates and BTSE-based films were obtained using a NEON 40 FE-SEM microscope (Carl Zeiss SMT AG, Oberkochen, Germany), which was equipped with an InLens and a SE2 detector. The EDX mapping was performed using different probe forming convergence semi-angles, which were taken each 35°, with the probe voltage set to 4 kV. The aperture was fixed to 120 μm, whereas the size of the frame was 256pixels × 192 pixels. 40 ms were used to record each pixel.

Polarization-modulation infrared reflection-absorption spectroscopy (PM-IRRAS)

The deposited organosilane-based thin films were characterized by using a Vertex 70 (Bruker Optics Germany) with an external PM-IRRAS set-up (p-polarization with an aluminum wire grid, which was modulated at 50 kHz with a ZnSe Photo-Elastic-Modulator (PMA50, Bruker Optics Germany), equipped with a ZnSe lens onto a cryogenic mercury cadmium telluride (LN-MCT) detector). The total number of scans was set as 1024, and the energy resolution was 2 cm^{-1}.

X-ray photoelectron spectroscopy (XPS)

XPS measurements were performed using an Omicron ESCA+ system (Omicron NanoTechnology GmbH) equipped with a hemispherical energy analyzer at a base pressure of $<5{\cdot}10^{-10}$ mbar. Spectra were recorded at pass energies of 100 eV for survey spectra and 20 eV for element spectra. A monochromatic Al Kα (1,486.3 eV) X-ray source with a spot diameter of 1 mm was used. The take-off angle of the detected photoelectrons was set to 60° in relation to the surface plane. Spectra were internally calibrated to the C1s peak (binding energy, BE = 285 eV). For peak fitting, a combination of Gaussian (70%) and Lorentzian (30%) distribution was used. Data analysis was performed with CASA-XPS software. Quantification was performed through integration of the peaks with respect to the corresponding relative sensitivity factor (RSF) values. A Shirley type background correction was used.

Electrochemical characterization

A three-electrode setup cell connected to a potentiostat-galvanostat Gamry 600^{TM} was used to carry out the electrochemical characterization of the substrates. Bare and BTSE-modified DC04 plates (2cm x 2 cm^2) acted as working electrodes, whereas a gold coil was used as counter electrode, and a commercial Ag/AgCl (3 M KCl, Radiometer Analytical), was employed as the reference electrode. The surface of the samples was exposed to the supporting electrolyte solution, namely an aerated borate buffer solution (0.2 M H_3BO_3, 0.05 M Na_2SO_4, 0.05 M $Na_2B_4O_7 \cdot 10\ H_2O$, 0.5 M NaCl, pH 8.4), and the open circuit potential

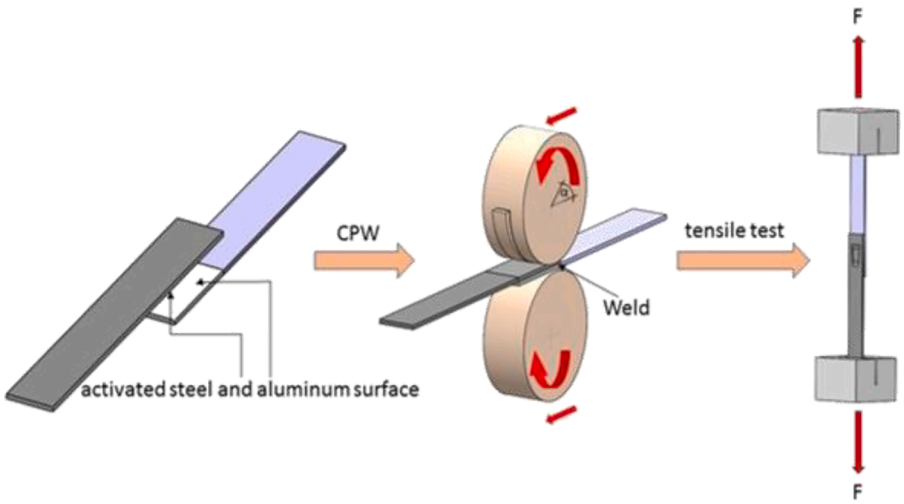

Fig. 1. Sketch showing the joining of steel and aluminum specimens by CPW and the assessment of their weld strength by tensile shear testing.

(OCP) was measured for 30 min. Afterwards, electrochemical impedance spectroscopy (EIS) measurements were performed in a frequency range from 100 kHz to 10 mHz with a signal amplitude perturbation of 10 mV. Potentiodynamic polarization curves were also registered after measuring the OCP for 30 min. These measurements were performed by scanning the applied potential from -1.0 V (vs. Ag/AgCl) to +1.0 V (vs. Ag/AgCl) at a scan rate of 2 $mV{\cdot}s^{-1}$. The corrosion potential E_{corr}, together with the corrosion current density i_{corr}, were obtained from the polarization curves by the Gamry software through Tafel slope extrapolation. The charge-transfer properties exhibited by these BTSE films were investigated by carrying out cyclic voltammetry measurements in a 0.1 M Bu_4NBF_4-containing ACN solution in the presence of an electrochemical redox probe, i.e., 2 mM of 2,4,6-triphenylpyrylium tetrafluoroborate. Ten consecutive cyclic voltammograms were registered for each sample at 50 $mV{\cdot}s^{-1}$.

Results and discussion

In order to shed light onto the mechanism related to the sol-gel deposition process on steel, cyclic voltammetry measurements were carried out for DC04 substrates immersed in different electrolyte-containing aqueous solutions. The data are displayed in Fig. S5a in the SI. The voltammograms show the typical electrochemical profile exhibited by iron electrodes, namely the multiple faradaic processes corresponding to the successive formation and reduction of the differential oxidation state iron oxyhydroxides, preceding the hydrogen evolution reaction (*HER*) (Díez-Pérez et al., 2001). It can be concluded that the overall result of applying a sufficiently negative cathodic potential (in the range of -1.2 V (vs. Ag/ AgCl)) in a NO_3^--containing aqueous solution at pH 4.5 is the local increase of the pH in the solid-liquid interface as a consequence of the occurrence of *HER* and the reduction reactions of O_2 and NO_3^- (Ait Ahmed et al., 2013).

Interestingly, when the previously hydrolysed BTSE water/ethanolic solution (pH 4.5) is made 0.2 M in $NaNO_3$, a broad featureless electrochemical response, but exhibiting a net cathodic current preceding *HER*, was detected, as can be seen in Fig. S5b in the SI. As previously stated, this net cathodic current should be attributed to the overlapping of *HER* and the reduction reactions of O_2 and NO_3^-. When 50 mM $Zn(NO_3)_2$ are added to the BTSE containing water/ethanolic solution (but maintaining constant the concentration of NO_3^- ions, i.e. 0.2 M, constant), a small diffusion-controlled irreversible faradaic peak, presumably corresponding to the electroreduction of Zn^{2+} ions to Zn(0), is clearly visible at -1.1 V (vs. Ag/ AgCl) (Ait Ahmed et al., 2013). Although not so evident, a small anodic hump can also be identified at -0.85 V (vs. Ag/ AgCl). Indeed, Cruz and co-workers have extensively studied the electrodeposition of Zn at different pH values (Vazquez-Arenas et al., 2012). According to the authors, the range potential range corresponding to the afore-mentioned peaks registered at pH = 4.5 is broadly matching with the Zn deposition and its ulterior reoxidation.

Considering the optimum window potential range deduced from Fig. S5 in the SI, BTSE and BTSE: Zn thin films were prepared on DC04 steel samples by chronoamperometry. Thus, normalized current density-time curves were registered for DC04 at -1.2 V (vs. Ag/ AgCl) and are displayed in Fig. 2. The latter exhibited the typical shape expected for electrodeposition processes characterized by an instantaneous nucleation followed by diffusion-limited growth according to the Scharifker–Hills model for nucleation and growth (Guo et al., 2011).

Higher diffusion-controlled current densities have been detected for the Zn^{2+}-containing precursor sol-gel solution, i.e., BTSE:Zn thin film, cf. the blue chronoamperogram in Fig. 2. This can be attributed to the occurrence of the co-deposition of metallic Zn nanoparticles as already pointed out by Wu et al. (2012).

High resolution FE-SEM and AFM images were registered before and after the modification of the activated DC04 steel surfaces with the nanocomposite films, i.e., BTSE and BTSE:Zn. Interestingly, BTSE sol-gel films prepared for short deposition times, namely $t = 5$ s, Fig. 3a and b,

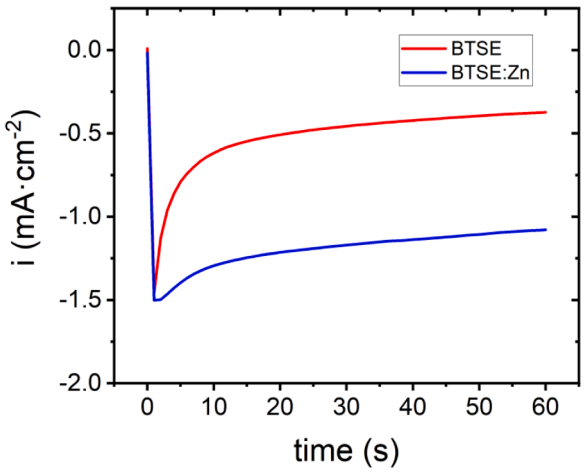

Fig. 2. Chronoamperometric curves registered for DC04 electrodes at -1.2 V (vs. Ag/ AgCl) for t=60 s in a 2.5 %(w/w) BTSE in a 75 %(v/v) ethanol/ Milli-Q water solution containing 0.2M in $NaNO_3$ (red line) and 50 mM $Zn(NO_3)_2{\cdot}6H2O$ (blue)

showed a grain-like structure which does not preclude from detecting the typical traits of the underlying steel substrates. The latter is indicative of the deposition of a very thin layer. Characteristic topographic features related to deposited BTSE:Zn thin films such as flake-like (for $t = 5$ s) and amorphous discontinuous (for $t = 60$ s) deposits could be detected in the FE-SEM images displayed in Fig. 3c-f. These can be attributed to the co-deposition and growth of metallic Zn particles in the nanocomposite films.

AFM measurements were carried out to characterize the topography of the steel samples before and after modification with the BTSE and the BTSE:Zn layers on the nanoscale. Fig. 4a shows the characteristic topographic features of a bare DC04 steel sample where a featureless surface can be distinguished. For a deposition time of $t = 5$s, AFM images show the formation of a sol-gel based granular electrodeposit consisting of smooth pancake-shaped island structures, which homogeneously covers the steel substrate. The latter are delimited by cracks, rifts, or defects in the film, which allow for the quantification of the thickness of the BTSE film (red-dashed circle depicted in Fig. 4b). Accordingly, by carrying out cross section profiles, the thickness of the layer could be estimated to be 3-6 nm, as can be seen in Fig. 4b. The origin of these cracks can be attributed to the incomplete bidimensional growth of the already formed sol-gel nuclei/ islands which can be attributed to the short deposition time used. Moreover, the occurrence of *HER* cannot be ruled out considering the applied potential range. Consequently, the formation of H_2 bubbles at the solid-liquid interface could be responsible for the observed cracked topographic features. Similar results have been observed for the result of the modification of the DC04 steel substrates with the BTSE:Zn layer, as can be appreciated in Fig. 4c. In this case, the presence of 3D-aggregates of rounded nanoparticles decorating the sol-gel film can be identified. In this regard, Fig. S6 in the SI shows the topographic details related to these clusters of rounded particles, ranging 3-8 nm high and 20-50 nm wide, as can be seen in the cross-section profile of Fig. S6a. These particles, which are not present in the BTSE layer, according to the phase contrast AFM image displayed in Fig. S6b, can be then attributed to Zn-rich particles. When the deposition time is increased, i.e., to t = 60 s, thicker and rougher films are obtained, as can be seen in the Fig. S7 in the SI.

The electrochemical deposition of BTSE and BTSE: Zn layers for $t = 5$ s can be also carried out onto AW1050A H111 surfaces and AFM imaging was performed in order to unveil their characteristic topographic features. The thin films deposited exhibit similar morphological profiles to those previously observed for DC04 samples, namely the formation of pancake-like islands, which homogeneously covers the aluminum

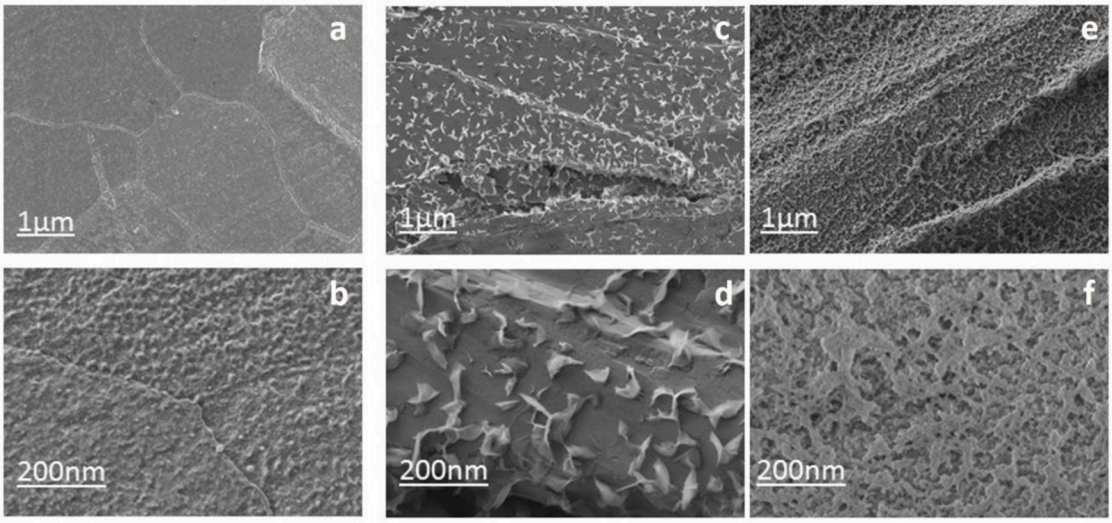

Fig. 3. FE-SEM images of DC04 steel samples after different surface conditioning processes: modification with BTSE for t= 5 s (a and b), modification with BTSE:Zn for t= 5 s (c and d), and modification with BTSE:Zn for t= 60 s (e and f)

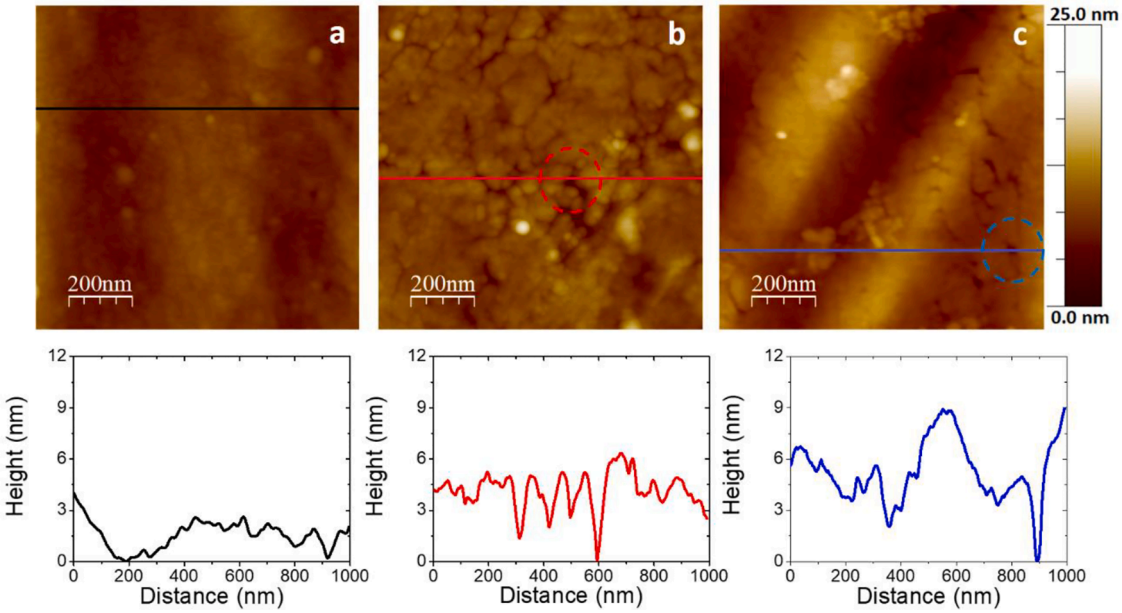

Fig. 4. 1.0 × 1.0 µm^2 AFM images of DC04 steel samples with different surface conditioning processes: 120 ground and subsequent dipping of into a 25 g/ L NaOH-containing aqueous solution for t = 1 min (a), modification with BTSE for t= 5 s (b), and modification with BTSE:Zn for t= 5 s (c) (top panel); representative cross section profiles show the dimensions of the corresponding BTSE deposits (bottom panel). Red and blue dashed circles indicate defect in the BTSE layer used for the quantification of the film thicknesses.

substrate as can be seen in the Fig. S8 in the SI. As previously mentioned, the occurrence of cracks and defects allows the quantification of the xerogel layer thickness. Thus, by performing cross section profiles through the cracks, a thickness range of 20 to 35 nm could be estimated. Interestingly, for the same deposition time, (t = 5 s), the BTSE layers deposited onto AW1050A H111 surfaces are noticeable thicker than those obtained for DC04 samples, with values around 3 to 6 nm. The deposition of the BTSE film is responsible for a noticeable decrease in the average *RMS* roughness from 22.2 to 14.6 nm. In this regard, Hu et al. has already reported efficient APTES and BTSE-based electrochemical deposition onto Al alloys (Jiang et al., 2012, 2015, 2015; Hu et al., 2006).

However, after the deposition of the BTSE:Zn layer, a rougher film incorporating some round shaped particles, 5 to10 nm high and 30 to 60 nm wide, randomly distributed over the surface forms, as can be observed in Fig. S8c. The thickness of the BTSE:Zn layer, as deduced from the cross-section profile and the fracture identified with a blue circle, would definitely be in the same range than that obtained for the BTSE layer obtained in the absence of Zn.

In order to obtain valuable information about the chemical composition of the BTSE-based modified steel surfaces, XPS measurements of the bare substrates before and after being modified with the sol-gel film, with or without Zn^{2+}, were carried out. The results obtained from the quantitative analysis of the corresponding survey spectra are summarized in Table 1. These data confirmed the evidence already pointed out by SEM and AFM, i.e., the DC04 substrates have been successfully modified by the BTSE and the BTSE:Zn composite films. Indeed, after the electrochemically induced deposition of the sol-gel, the presence of the

Table 1
XPS surface composition analysis of DC04 steel substrates, after the corresponding surface treatments (successive solvent cleaning, 120 grit size grinding and NaOH activation for steel and solvent cleaning and pickling for aluminum), and after BTSE and BTSE:Zn thin film deposition + thermal annealing at 120°C for 15 min, based on XPS survey spectra (Fig. S9 in the SI) in at. % for the different surface states.

Sample	Element (at. %)					
	C	O	Si	Zn	Fe	Al
DC04	26.2	37.7	-	-	35.1	-
DC04 + BTSE t = 5s	27.2	38.9	23.3	-	10.6	-
DC04 + BTSE:Zn t = 5s	23.2	37.5	24.9	1.6	12.8	-

BTSE or the BTSE:Zn layers was further confirmed by the appearance of the corresponding Si 2p, or Si 2p and Zn $2p_{3/2}$ signals, respectively.

Deeper characterization of the surface chemistry for the as-prepared BTSE-modified substrates was carried out by means of the assessment of the high-resolution core level spectra of C 1s, Si 2p and Zn $2p_{3/2}$ depicted in Fig. 5. The presence of C-Si, C-O-Si, and Si-O-Si bonds accounts for the successful functionalization of DC04 surface with the thin organosilane film. Only residual amounts of N are detected indicating that $Zn(NO_3)_2$ and $NaNO_3$ leftovers are swept after successive rinsing in ethanol and Milli-Q water. The C1s peak has been fitted according to three different components at 284.6, 286.1, and 288.5 eV, Fig. 5a. The latter components were then attributed to C-Si, C-C, and C-H groups (284.6 eV), C-OH, C-O-Si and C-O-C (286.1 eV), and finally C=O or O-C=O groups (288.5 eV), respectively (Parhizkar et al., 2017; Graf et al., 2009). Adventitious carbon and the deposition of the BTSE film would be responsible for these contributions.

The Si 2p spectrum could be fitted to one single component at 102.6 eV, Fig. 5b. The latter corresponds to monoalkylsilane, C-SiO_3, siloxane, C-$Si(OSi)_3$, groups, Si–O–Si, Si–OH or Si–O–metal bonds (Dietrich et al., 2016; Quiroga Argañaraz et al., 2015).

As can be observed in the high-resolution spectrum depicted in Fig. 5c, the Zn $2p_{3/2}$ peaks appear centered at 1021.5 eV which has been largely attributed to ZnO (Fink et al., 2006). Most importantly, a small contribution at 1020.2 eV was also found. The latter has been assigned to metallic Zn, confirming thus the co-deposition of metallic Zn during the thin-film formation reaction and its subsequent oxidation to ZnO under ambient conditions (Wu et al., 2012; Fink et al., 2006). Analogue results have been recently reported by Wu et al. for the co-deposition of BTSE and Zn on cold-rolled steel surfaces (Wu et al., 2012). Paying attention to the results deduced form the survey spectra summarized in Table 1, only reduced amounts of co-deposited ZnO particles are obtained for short deposition times (t = 5 s), namely 1-2 %. Indeed, the analysis of the fractional surface coverage of 3D-aggregates of ZnO particles, extracted from AFM images shown in Fig. 4 turned out to be ≈ 5-10 %. As expected, for higher deposition times, t = 60 s, the Zn at. % increased to ≈4 % (see Fig. 7 in the SI).

Additionally, a PM-IRRAS analysis was performed on DC04 steel samples modified with the nanocomposite films.

The PM-IRRAS data of BTSE and BTSE:Zn films prepared for a deposition time of t = 5 s are displayed in Fig. 6. The contributions appearing at 2860 and 2916 cm^{-1} correspond to the symmetric and asymmetric C-H vibration modes, respectively, from -CH_2 groups corresponding to the aliphatic backbone in the BTSE molecule (Quiroga Argañaraz et al., 2015). The peak at 1280 cm^{-1} is assigned to Si-C symmetric bending (Jiang et al., 2012). The peaks arising at 916 and 1127 cm^{-1} are attributed to silanol (Si-OH) and Si-O-Si groups present in the film (Huser et al., 2013). The presence of the former is crucial for the promotion of the formation of Si–O–Al bonds in CPW processes to aluminum counterparts, while the latter would account for the successful cross-linking within the silicone-like matrix occurred during the curing process (15 minutes at 120 °C). In the case of BTSE:Zn partial overlapping between this Si-O-Si peak and the Zn-OH peak was

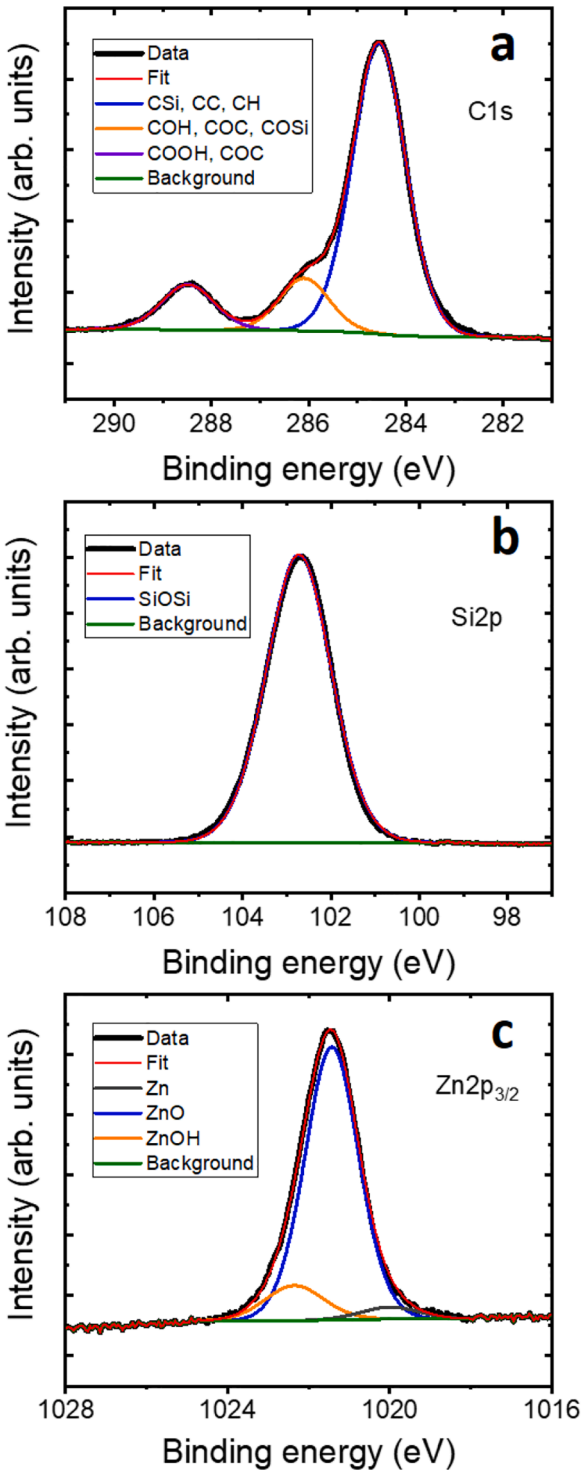

Fig. 5. High resolution core-level spectra registered for BTSE:Zn layers deposited at -1.2 V (vs. Ag/ AgCl) for t = 5 s onto DC04 steel substrates: C1s (a), Si2p (b), and Zn$2p_{3/2}$ (c).

detected, with the subsequent shift of the maximum peak to lower wavenumbers, i.e., 1088 cm^{-1} (Hoppe et al., 2016; Fink et al., 2006).

Taking into account the aforementioned results, the mechanism for the electrografting of the BTSE-based film can be summarized as follows. The first step consists of the hydrolysis of methoxy groups to silanol groups (Si-OH) which is catalyzed in slightly acidic water-ethanol solutions. These silanols interact with the hydroxyl-rich oxide covered steel surface by means of hydrogen bonding (i). When a sufficiently

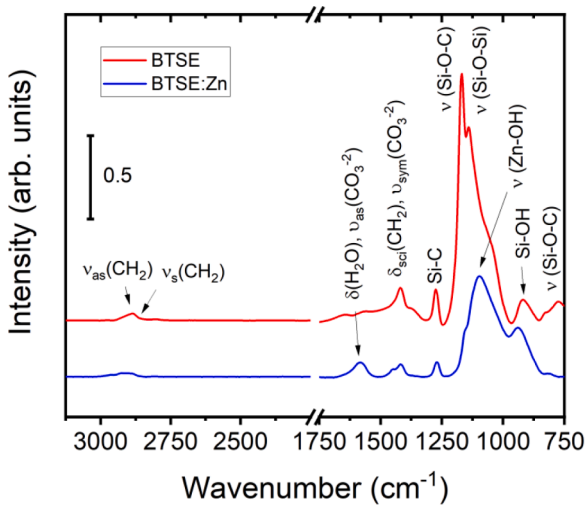

Fig. 6. PM-IRRAS spectrum registered for a DC04 steel substrate modified with BTSE (red line) and BTSE:Zn (blue) prepared for a deposition time of t = 5s at -1.2 V (vs. Ag/ AgCl)

negative potential is applied, both the reduction of nitrate to nitrite groups, and/ or H^+ or dissolved oxygen, is accompanied by the generation of hydroxyl anions, which results in the local increase of the pH in the vicinity of the electrode. Thus, a condensation reaction takes place with the subsequent grafting of the film to the steel surface, i.e. electrografting (ii). These steps are summarized in Fig. 7 presented below. By curing (water removal), the cross-linking process is promoted (iii). Moreover, the formation of Si-O-Me bonds becomes more likely when the water activity in the interface is reduced during the curing process. When the electrochemically induced condensation reaction is carried out in a Zn^{2+}-containing electrolyte, the co-deposition of small metallic Zn particles (rapidly oxidized to ZnO under ambient conditions) can take place as well (iv), as schematically proposed in Fig. S10 in the SI.

Electrochemical characterization

The charge transfer barrier capabilities exerted by the BTSE and BTSE:Zn thin films have been characterized by registering cyclic voltammograms in the presence of an electrochemical redox probe, namely 2,4,6 triphenylthiopyrylium in ACN. The latter has been successfully employed by Daasbjerg and co-workers to assess the charge transfer properties of polyphenylene-based thin films prepared by electroreduction of aryldiazonium salts on steel surfaces (Hinge et al., 2010). Fig. 8 shows the current density-potential (i-E) curves collected for the bare DC04 and BTSE and BTSE:Zn thin films deposited on DC04 steel substrates (after curing for 15 min at 120 °C). The two-peaked quasi-reversible and diffusion-controlled electrochemical profile exhibited by the former can be attributed to the oxidation/ reduction reactions of the electrochemical redox probe which shows a peak-to-peak separation of about 200 mV. After the electrochemically assisted deposition of the BTSE and BTSE:Zn films for $t = 5$ s (red and blue voltammograms in Fig. 8a, respectively), a noticeable increase in the peak-to-peak separation, accompanied by a decrease in the current densities measured, can be observed in the cyclic voltammograms of the latter. The overall effect can be explained in terms of the limited diffusion of the electrochemical redox probe through the as-prepared sol-gel films. Interestingly, this fact is more pronounced for the case of the BTSE:Zn thin films, indicating thus the formation of a denser and more compact sol-gel layer when the Zn^{2+}-containing working electrolyte is employed, via either catalysis of the sol-gel process by Zn^{2+} ions and/ or the co-deposition of Zn metallic particles. As can be deduced from Fig. 8b, when longer deposition times are applied, i.e., $t = 60$ s, the charge-transfer blocking properties of the BTSE and BTSE:Zn films are significantly boosted. Thus, higher peak-to-peak separations and lower current densities are observed, which is attributed to the formation of thicker films with a low density of defects and pinholes.

Potentiodynamic polarization curves were also obtained for a

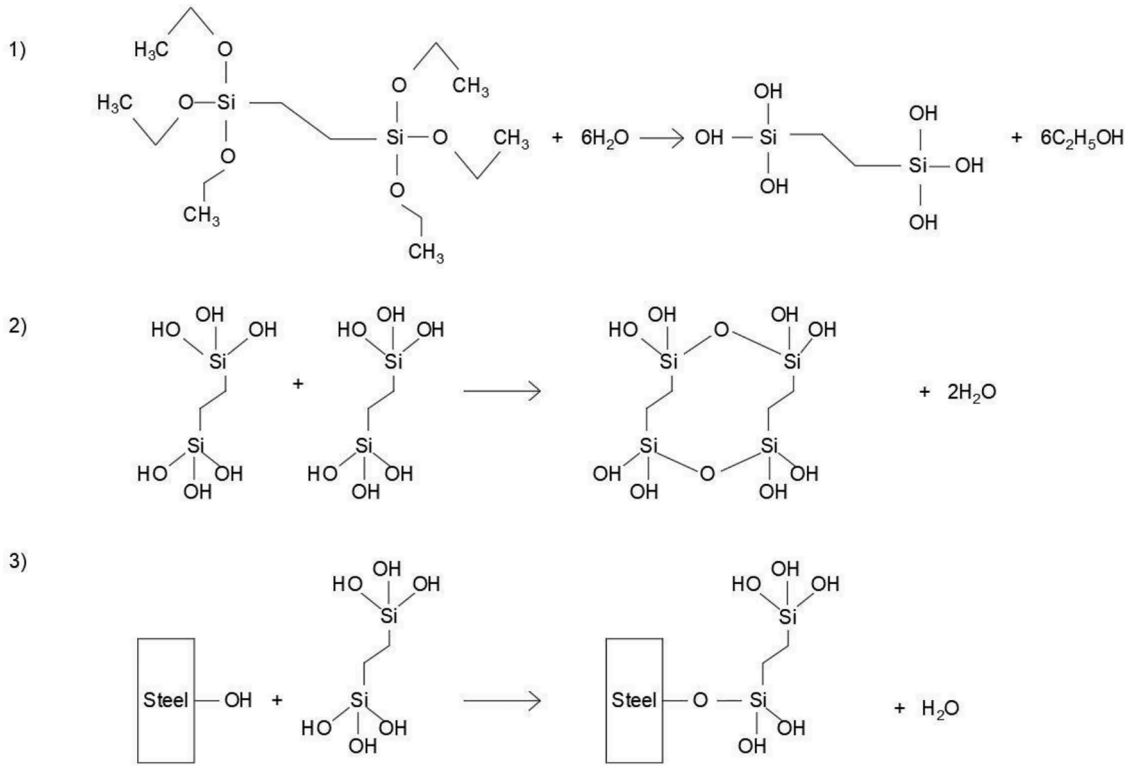

Fig. 7. Sketch showing the different steps involved in the electrografting of the BTSE-based sol-gel thin film.

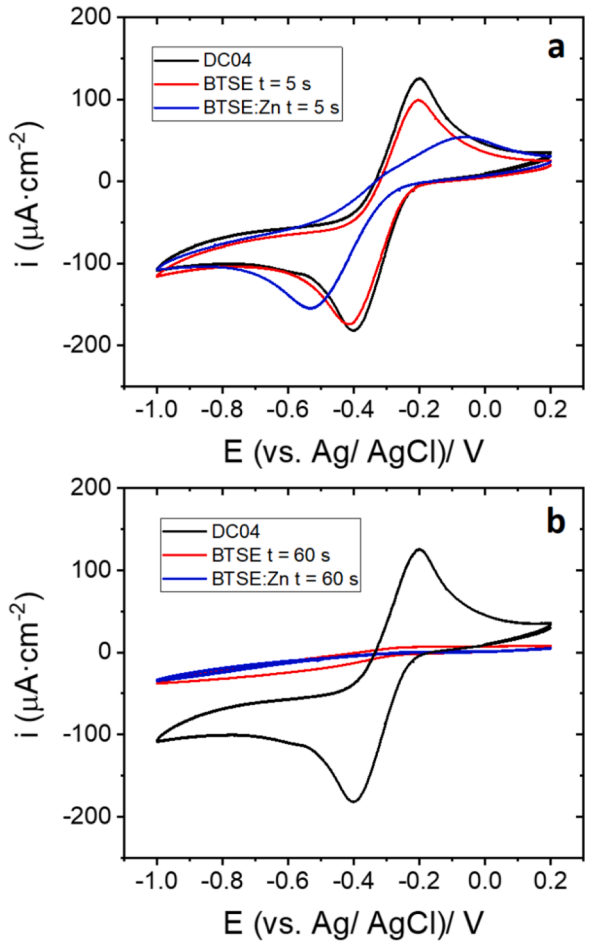

Fig. 8. Cyclic voltammograms registered for the bare DC04 (black line), BTSE (red), and BTSE:Zn (blue) in a 2 mM 2,4,6 triphenylthiopyrylium-containing 0.1 M Bu_4NBF_4/ ACN at 0.05 $V{\cdot}s^{-1}$ for a deposition time of t = 5 s (a) and 60 s (b).

broader characterization of the electrochemical properties of the BTSE and BTSE:Zn films and the data are displayed in Fig. 9. The E_{corr} values registered for BTSE film covered substrates prepared for different deposition times (t = 5 and 60 s) are shifted to more negative potentials

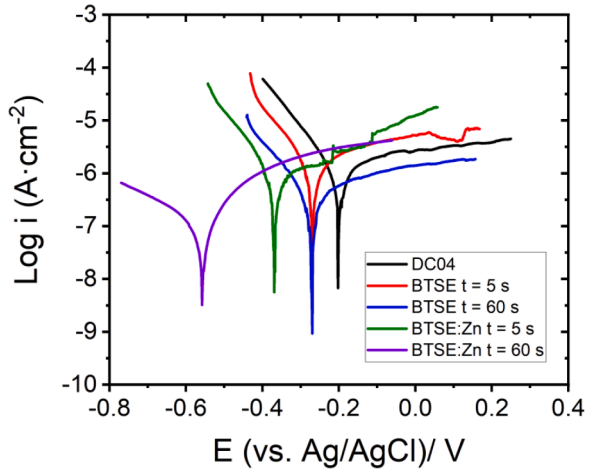

Fig. 9. Potentiodynamic polarization curves registered in aerated buffer solution (pH 8.4) at 2 $mV{\cdot}s^{-1}$ for the bare DC04 (black curve) and BTSE (red for t = 5 s and blue for t = 60 s) and BTSE:Zn (green for t = 5 s, green, and t = 60 s, purple) films prepared for different deposition times.

in comparison to that exhibited by the bare DC04. This has been already reported by Wu et al. and can be justified in terms of the higher overpotentials required by the *ORR* to occur (Wu et al., 2012).

As expected, longer deposition times imply lower corrosion current densities which is indicative of the formation of a thicker film with a lower density of defects or pinholes, as can be deduced from the blue curve in Fig. 9.

When Zn/ZnO particles are incorporated, cf. the green and purple curves in Fig. 9, the OCP values move to even more negative values indicating cathodic protection due to their sacrificial anode behavior (green curve). Lower exchange current densities are consequently detected when thicker and low-defective films are obtained for longer deposition times (blue curve). The corresponding values registered for E_{corr} and j_{corr} are displayed in Table 2.

The corrosion protection barrier properties of these BTSE-based films were studied by means of EIS measurements carried out for different immersion times in an aerated borate buffer electrolyte solution. The corresponding Bode and low frequency impedance modulus versus time plots registered for both BTSE and BTSE:Zn thin films for different deposition times (t = 5 and 60 s) are displayed in Figs. S11 and S12 in the SI, respectively. In all the cases, the impedance values measured for the bare substrates were lower than those registered for the nanocomposite film coated steel substrates indicating the corrosion inhibition effect due to the barrier properties of the siloxane film. The progressive increase in the impedance modulus with the immersion times observed herein can be justified in terms of the formation of a robust three dimensionally crosslinked Si-O-Si matrix firmly attached to the steel surface, together with the formation of corrosion products, hindering electrolyte diffusion. Interestingly, these values are even higher when ZnO nanoparticles are present in the film, which would account for an additional protection.

Interfacial bonding and tensile shear test

Fig. 10a displays characteristic tensile shear curves registered for the different combinations of welded specimens DC04/ BTSE-based thin film/ AW1050A H111 collected herein and after the different heating treatments. The averaged values corresponding to the maximum shear force registered for the as-prepared welded specimens were plotted in Fig. 10b. The reference, i.e., DC04 steel substrates (ground to P120 grit size paper) welded to pickled EN AW-1050 A H111 aluminum, exhibited maximum shear forces in the range of 700 N and 705 N for those heated at 200°C (DC04 200°C).

Some considerations must be taken into account: No significant differences in weld strength could be found for the reference specimens before and after thermal treatments at 200 °C or 400 °C (i), and the maximum shear force values registered for joinings using BTSE and BTSE:Zn-modified DC04 specimens were not statistically distinct from the reference when no thermal treatment was applied (ii). Still, the results summarized in Fig. 10 is clearly showing that BTSE-based coatings provide noticeably increased values of shear strength in comparison with that from the reference samples after the thermal treatment at 200 °C. The BTSE and BTSE:Zn coatings did not show drastic differences in weld strength, but slightly higher values could be observed when Zn metallic particles were present in the nanocomposite film. Interestingly,

Table 2
E_{corr} and j_{corr} estimated from the potentiodynamic polarization curves displayed in Fig. 9 by extrapolation of Tafel plots.

Sample	E_{corr} (vs. Ag/AgCl)/ V	i_{corr}/ $A{\cdot}cm^{-2}$
DC04	-0.204	$9.77{\cdot}10^{-7}$
BTSE (t = 5 s)	-0.271	$5.37{\cdot}10^{-7}$
BTSE (t = 60 s)	-0.271	$1.48{\cdot}10^{-7}$
BTSE:Zn (t = 5 s)	-0.368	$3.47{\cdot}10^{-7}$
BTSE:Zn (t = 60 s)	-0.556	$1.07{\cdot}10^{-7}$

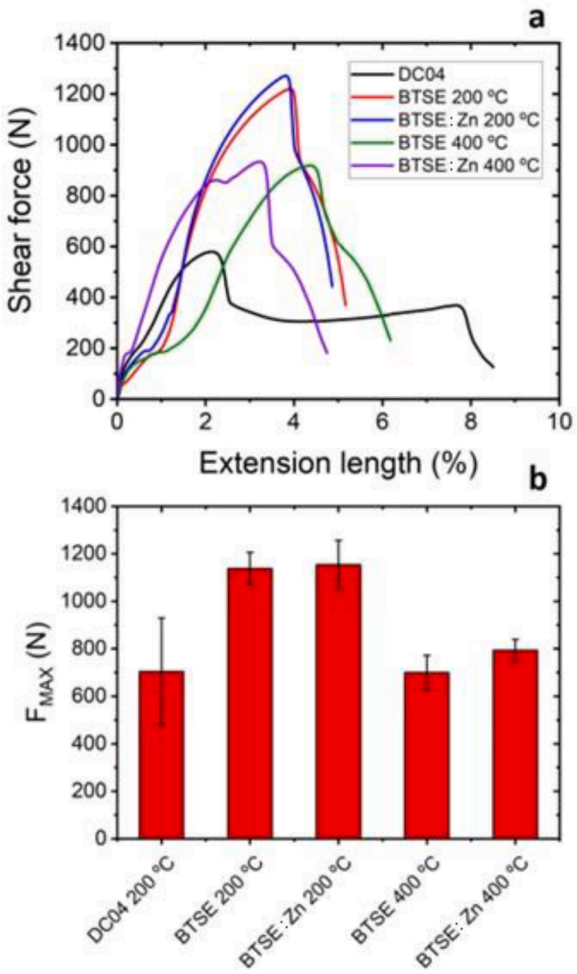

Fig. 10. Characteristic shear force vs. extension curves (a) and averaged maximum shear force (b) registered for joining specimens welded by CPW between pickled AW1050A H111 and bare DC04 and BTSE and BTSE/ Zn-modified DC04 steel substrates at 200 °C or 400 °C (thickness reduction 75 %).

although Gandhi et al. (2007). argued that, at temperatures ≥400 °C the irreversible formation of siloxane bridges with hydroxyl groups at the oxide surface by dehydration occurs, the best results were obtained herein for 200 °C, as already shown by Hoppe et al. for a MPTS SAM interlayer in copper-aluminum joinings (Hoppe et al., 2016). In this regard, Grundmeier and co-workers had showed already that higher applied temperatures dropped weld strengths in the joining between steel and aluminum by CPW (Hoppe et al., 2016).

The promotion of the enhanced interfacial bonding measured herein can be explained as follows: the welding of DC04 and AW1050A H111 counterparts by CPW is based on the extrusion of virgin metallic material through the cracked oxide layers by plastic deformation. Thus, metal-to-metal bonds between the welded metallic surfaces are produced (i). The electrografting of a composite thin film covalently bound to the steel surface is achieved by the electrochemically assisted condensation between silanol groups in the sol-gel and the hydroxyl groups at the metal oxide interface (ii). After curing, the polycondensation of Si-O-Si groups within the films occurs (iii). Once the BTSE-modified steel substrates is welded to the aluminum counterpart by CPW, remaining silanol groups on the surface of the siloxane layer react with the hydroxyl-rich aluminum oxide surface, which is promoted by thermal annealing at 200 °C (Gandhi et al., 2007). A bifunctional BTSE-based layer covalently bound to both metal oxide surfaces is consequently obtained, reinforcing thus the interfacial bonding in the joint (iv). These steps are summarized in Fig. 11.

It is worth noting that the formation of intermetallic particles at high temperatures, for instance Fe-Zn in galvanized steel, has been proven to increase the shear forces of welded joints (Hordych et al., 2016, 2018, 2019). The FE-SEM analysis of FIB cross sections displayed in Fig. S13 in the SI, accompanied by the corresponding EDX profiles, shows that no intermetallic Fe-Al phases were formed after the thermal treatment at 200 °C. This confirms that the adhesion-promoting capabilities of the as-deposited BTSE-based nanocomposite thin films is mostly responsible for the enhanced values of the maximum shear force observed in Fig. 10. Nevertheless, the slightly higher figures registered for BTSE:Zn films in comparison to BTSE might be tentatively explained in terms of the formation of intermetallic Fe-Zn nanoparticles at the solid oxides interface.

The plastic deformation process occurring at the interface between steel and aluminum specimens as a consequence of the CPW were also investigated. With this aim, SEM and EDX measurements were carried out after tensile shear testing. Fig. S14 in the SI shows FE-SEM images of the DC04 steel surfaces after fracture upon tensile testing. The deformation of the polishing lines due to the caused stress and plastic deformations can be noticed. A detailed EDX-mapping analysis of the DC04 steel substrates measured after tensile shear testing is displayed in Fig. S15 and shows a noticeable presence of transferred Al oxide patches. This resembles the characteristic topographical features produced after pickling depicted in Figs. S3 and S4 in the SI. The latter were found in considerably lower extent on the blank specimens, see Fig. S14 in the SI. This accounts for an effective bonding support between the two oxide layers exerted by the electrografted BTSE film. The steel/Al joint failure mechanism is presumably a consequence of the combination of ductile and brittle fracture processes. Thus, the ductile fracture would mostly take place at the extruded material joints leaving grooves and defects or pinholes on the surface, as can be seen in Fig. S14 in the SI. Nevertheless, the brittle fracture would occur in a larger extension when BTSE and

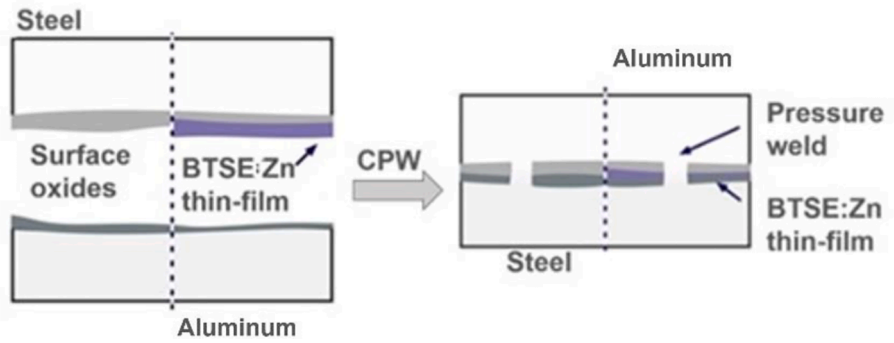

Fig. 11. Sketch showing the extrusion by plastic deformation of virgin metallic material through the (thin)cracked oxide layers and the subsequent formation of metal-to-metal bonds. In the interspace with opposed metallic oxide layers, the bonding is reinforced by means of the bifunctional composite matrix which is covalently bound to both hydroxyl-rich metal oxide surfaces.

BTSE:Zn thin films were present, since a strong interfacial adhesion, attributed to covalent bonding between metal oxide layers, is promoted. In this case, cracks may propagate preferably through the metal/metal oxide layers rather than along the interface. This proposed mechanism might tentatively explain rather large area patches of Al on the steel surface, as can be observed in Fig. S15 in the SI.

Conclusions

In the present study, the influence of electrochemical conditioning and a combination of mechanical and electrochemical surface modification procedures of both steel and aluminum specimens by means of binding enhancement between the two metals after CPW were investigated. A successful surface modification with electrochemical deposition of BTSE-based thin films for different deposition times could be demonstrated by means of different spectroscopic and electrochemical methods. Data extracted from XP and PM-IRRA spectra have shown a good agreement of the results. Accordingly, both techniques could prove the formation of the BTSE-based thin layers on the steel surface. The electrochemical OCP measurements have shown that when the steel substrates are modified with the BTSE:Zn layer, a noticeable shift to more negative potentials can be observed. The latter is explained in terms of the corrosion cathodic protection due to the presence of Zn component of the BTSE: Zn composite layer. Characteristic topographic features were shown by means of AFM measurements on a bare 120 grit size ground DC04 substrate, namely a featureless, nanostructured surface. AFM images show, for lower deposition times, namely t= 5s, the formation of a BTSE-based granular electrodeposit consisting of smooth grain-like polymer structures, which homogeneously covers the steel substrate. It was found that the thin BTSE coatings (deposition time t= 5 s) on steel surfaces after welding with pickled aluminum are promoting better binding after CPW than the samples without BTSE coatings. The tensile tests have shown a significant increase in the tensile forces, in comparison with the blank, of ≈ 75%. The SEM and EDX measurements have shown that the extrusion of virgin material through cracks in the oxyhydroxide layers occurs, by means of plastic deformation, giving rise to metallic-bound areas. Moreover, the EIS results have shown an exalted corrosion resistance measured for the DC04 samples after being modified with the organo-silane layer which can be attributed to the barrier role played by the latter.

Declaration of Competing Interest

The authors declare that they have no known competing financial interests or personal relationships that could have appeared to influence the work reported in this paper.

Data availability

Data will be made available on request.

Acknowledgement

The authors thank the German Research Foundation (DFG) for their financial support of the ‘ECUF’ project (27635593) within the SPP 1640 framework. J.C.C. thanks to Universidad de La Laguna for his Research Contract UNI/551/2021 “María Zambrano”. A.G.O. thanks NANOtec, INTec and ULL for laboratory facilities.

Supplementary materials

Supplementary material associated with this article can be found, in the online version, at doi:10.1016/j.jajp.2022.100137.

References

Ait Ahmed, N., Eyraud, M., Hammache, H., Vacandio, F., Sam, S., Gabouze, N., Knauth, P., Pelzer, K., Djenizian, T., 2013. New insight into the mechanism of cathodic electrodeposition of zinc oxide thin films onto vitreous carbon. Electrochim. Acta 94, 238–244.
Atabaki, M.M., Nikodinovski, M., Chenier, P., Ma, J., Harooni, M., Kovacevic, R., 2014. Welding of aluminum alloys to steels: an overview. J. Manuf. Sci. Prod. 14 (2), 59–78.
Bay, N., 1979. Cold Pressure Welding—the mechanisms governing bonding. J. Eng. Ind. 101 (2), 121–127.
Bay, N., 1983. Welding J. 2, 137.
Bay, N., Clemensen, C., Juelstorp, O., Wanheim, T., 1985. Bond strength in cold roll bonding. CIRP Ann. 34 (1), 221–224.
Collinson, M.M., Howells, A.R., 2000. Peer Reviewed: sol–gels and electrochemistry: research at the intersection. Anal. Chem. 72 (21), 702. A-709 A.
Dietrich, P.M., Glamsch, S., Ehlert, C., Lippitz, A., Kulak, N., Unger, W.E.S., 2016. Synchrotron-radiation XPS analysis of ultra-thin silane films: Specifying the organic silicon. Appl. Surf. Sci. 363, 406–411.
Díez-Pérez, I., Gorostiza, P., Sanz, F., Müller, C., 2001. First Stages of Electrochemical Growth of the Passive Film on Iron. J. Electrochem. Soc. 148 (8), B307–B313.
Ebbert, C., Schmidt, H.C., Rodman, D., Nürnberger, F., Homberg, W., Maier, H.J., Grundmeier, G., 2014. Joining with electrochemical support (ECUF): Cold pressure welding of copper. J. Mater. Process. Technol. 214 (10), 2179–2187.
Fink, N., Wilson, B., Grundmeier, G., 2006. Formation of ultra-thin amorphous conversion films on zinc alloy coatings: Part 1. Composition and reactivity of native oxides on ZnAl (0.05%) coatings. Electrochim. Acta 51 (14), 2956–2963.
Gandhi, D.D., Lane, M., Zhou, Y., Singh, A.P., Nayak, S., Tisch, U., Eizenberg, M., Ramanath, G., 2007. Annealing-induced interfacial toughening using a molecular nanolayer. Nature 447, 299.
Gharagozlou, M., Naderi, R., Baradaran, Z., 2016. Effect of synthesized NiFe2O4-silica nanocomposite on the performance of an ecofriendly silane sol–gel coating. Prog. Org. Coat. 90, 407–413.
Goux, A., Etienne, M., Aubert, E., Lecomte, C., Ghanbaja, J., Walcarius, A., 2009. Oriented Mesoporous Silica Films Obtained by Electro-Assisted Self-Assembly (EASA). Chem. Mater. 21 (4), 731–741.
Graf, N., Yegen, E., Gross, T., Lippitz, A., Weigel, W., Krakert, S., Terfort, A., Unger, W.E. S., 2009. XPS and NEXAFS studies of aliphatic and aromatic amine species on functionalized surfaces. Surf. Sci. 603 (18), 2849–2860.
Guo, L., Oskam, G., Radisic, A., Hoffmann, P.M., Searson, P.C., 2011. Island growth in electrodeposition. J. Phys. D 44 (44), 443001.
Hinge, M., Gonçalves, E.S., Pedersen, S.U., Daasbjerg, K., 2010. On the electrografting of stainless steel from para-substituted aryldiazonium salts and the thermal stability of the grafted layer. Surf. Coat. Technol. 205 (3), 820–827.
Hoppe, C., Ebbert, C., Grothe, R., Schmidt, H.C., Hordych, I., Homberg, W., Maier, H.J., Grundmeier, G., 2016. Influence of the surface and heat treatment on the bond strength of galvanized steel/aluminum composites joined by plastic deformation. Adv. Eng. Mater. 18 (8), 1371–1380.
Hoppe, C., Ebbert, C., Voigt, M., Schmidt, H.C., Rodman, D., Homberg, W., Maier, H.J., Grundmeier, G., 2016. Molecular engineering of aluminum–copper interfaces for joining by plastic deformation. Adv. Eng. Mater. 18 (6), 1066–1074.
Hordych, I., Herbst, S., Nürnberger, F., Schmidt, H.C., Orive, A.G., Homberg, W., Grundmeier, G., Maier, H.J., 2019. The role of heat-treatments performed before and after a cold roll bonding process of galvanized steel sheets. AIP Conf. Proc. 2113 (1), 050017.
Hordych, I., Rodman, D., Nürnberger, F., Hoppe, C., Schmidt, H.C., Grundmeier, G., Homberg, W., Maier, H.J., 2016. Effect of pre-rolling heat treatments on the bond strength of cladded galvanized steels in a cold roll bonding process. Steel Res. Int. 87 (12), 1619–1626.
Hordych, I., Rodman, D., Nürnberger, F., Schmidt, H.C., Orive, A.G., Homberg, W., Grundmeier, G., Maier, H.J., 2018. Influence of heat-pretreatments on the microstructural and mechanical properties of galfan-coated metal bonds. AIP Conf. Proc. 1960 (1), 040007.
Hu, J.-M., Liu, L., Zhang, J.-Q., Cao, C.-N., 2006. Effects of electrodeposition potential on the corrosion properties of bis-1,2-[triethoxysilyl] ethane films on aluminum alloy. Electrochim. Acta 51 (19), 3944–3949.
Huser, J., Bistac, S., Brogly, M., Delaite, C., Lasuye, T., Stasik, B., 2013. Investigation on the adsorption of alkoxysilanes on stainless steel. Appl. Spectrosc. 67 (11), 1308–1314.
Ikjoo, B., Anthony, W.C., Beomjoon, K., 2013. Transfer of thin Au films to polydimethylsiloxane (PDMS) with reliable bonding using (3-mercaptopropyl) trimethoxysilane (MPTMS) as a molecular adhesive. J. Micromech. Microeng. 23 (8), 085016.
Jiang, L.-L., Wu, L.-K., Hu, J.-M., Zhang, J.-Q., Cao, C.-N., 2012. Electrodeposition of protective organosilane films from a thin layer of precursor solution. Corros. Sci. 60, 309–313.
Jiang, M.-Y., Wu, L.-K., Hu, J.-M., Zhang, J.-Q., 2015. Silane-incorporated epoxy coatings on aluminum alloy (AA2024). Part 2: Mechanistic investigations. Corros. Sci. 92, 127–135.
Jiang, M.-Y., Wu, L.-K., Hu, J.-M., Zhang, J.-Q., 2015. Silane-incorporated epoxy coatings on aluminum alloy (AA2024). Part 1: Improved corrosion performance. Corros. Sci. 92, 118–126.
Jin, X.-Z., Tsoi, J.K.-H., Matinlinna, J.P., 2019. A novel silane system for amalgam repair with resin composite: an in vitro Study. Silicon 11 (5), 2321–2331.
Li, L., Nagai, K., Yin, F., 2008. Progress in cold roll bonding of metals. Sci. Technol. Adv. Mater. 9 (2), 023001.

Liu, Y.-H., Jin, X.-H., Hu, J.-M., 2016. Electrodeposited silica films post-treated with organosilane coupling agent as the pretreatment layers of organic coating system. Corros. Sci. 106 (Supplement C), 127–136.
Luna-Vera, F., Dong, D., Hamze, R., Liu, S., Collinson, M.M., 2012. Electroassisted fabrication of free-standing silica structures of micrometer size. Chem. Mater. 24 (12), 2265–2273.
Matinlinna, J.P., Lassila, L.V.J., Vallittu, P.K., 2006. The effect of three silane coupling agents and their blends with a cross-linker silane on bonding a bis-GMA resin to silicatized titanium (a novel silane system). J. Dent. 34 (10), 740–746.
Meschut, G., Merklein, M., Brosius, A., Drummer, D., Fratini, L., Füssel, U., Gude, M., Homberg, W., Martins, P.A.F., Bobbert, M., Lechner, M., Kupfer, R., Gröger, B., Han, D., Kalich, J., Kappe, F., Kleffel, T., Köhler, D., Kuball, C.M., Popp, J., Römisch, D., Troschitz, J., Wischer, C., Wituschek, S., Wolf, M., 2022. Review on mechanical joining by plastic deformation. J. Adv. Join. Process. 5, 100113.
Mori, K.-i., Abe, Y., 2018. A review on mechanical joining of aluminium and high strength steel sheets by plastic deformation. Int J 1 (1), 1–11.
Mori, K.-i., Bay, N., Fratini, L., Micari, F., Tekkaya, A.E., 2013. Joining by plastic deformation. CIRP Ann. 62 (2), 673–694.
Parhizkar, N., Ramezanzadeh, B., Shahrabi, T., 2018. Corrosion protection and adhesion properties of the epoxy coating applied on the steel substrate pre-treated by a sol-gel based silane coating filled with amino and isocyanate silane functionalized graphene oxide nanosheets. Appl. Surf. Sci. 439, 45–59.
Parhizkar, N., Shahrabi, T., Ramezanzadeh, B., 2017. A new approach for enhancement of the corrosion protection properties and interfacial adhesion bonds between the epoxy coating and steel substrate through surface treatment by covalently modified amino functionalized graphene oxide film. Corros. Sci. 123, 55–75.
Pujari, S.P., Scheres, L., Marcelis, A.T.M., Zuilhof, H., 2014. Covalent surface modification of oxide surfaces. Angew. Chem. Int. Ed. 53 (25), 6322–6356.
Quiroga Argañaraz, M.P., Ramallo-López, J.M., Benítez, G., Rubert, A., Prieto, E.D., Gassa, L.M., Salvarezza, R.C., Vela, M.E., 2015. Optimization of the surface properties of nanostructured Ni–W alloys on steel by a mixed silane layer. Phys. Chem. Chem. Phys. 17 (21), 14201–14207.
Sayen, S., Walcarius, A., 2003. Electro-assisted generation of functionalized silica films on gold. Electrochem. Commun. 5 (4), 341–348.
Schmidt, H.C., 2018. Ein Beitrag zum stoffschlüssigen Fügen durch plastische Deformation: partielles Kaltpressschweißen durch inkrementelles Walzen. University of Paderborn. Dr.-Ing. Dissertation.
Schmidt, H.C., Homberg, W., Hoppe, C., Grundmeier, G., Hordych, I., Maier, H.J., 2016. Cold pressure welding by incremental rolling: deformation zone analysis. AIP Conf. Proc. 1769 (1), 100013.
Schmidt, H.C., Homberg, W., Orive, A.G., Grundmeier, G., Duderija, B., Hordych, I., Herbst, S., Nürnberger, F., Maier, H.J., 2019. Joining of blanks by cold pressure welding: Incremental rolling and strategies for surface activation and heat treatment. Materialwiss. Werkstofftech. 50 (8), 924–939.
Schmidt, H.C., Homberg, W., Orive, A.G., Grundmeier, G., Hordych, I., Maier, H.J., 2018. Cold pressure welding of aluminium-steel blanks: Manufacturing process and electrochemical surface preparation. AIP Conf. Proc. 1960 (1), 050007.
Shacham, R., Avnir, D., Mandler, D., 1999. Electrodeposition of Methylated Sol-Gel Films on Conducting Surfaces. Adv. Mater. 11 (5), 384–388.
Toledano, R., Mandler, D., 2010. Electrochemical Codeposition of Thin Gold Nanoparticles/Sol−Gel Nanocomposite Films. Chem. Mater. 22 (13), 3943–3951.
Vazquez-Arenas, J., Sosa-Rodriguez, F., Lazaro, I., Cruz, R., 2012. Thermodynamic and electrochemistry analysis of the zinc electrodeposition in NH4Cl–NH3 electrolytes on Ti, Glassy Carbon and 316L Stainless Steel. Electrochim. Acta 79, 109–116.
Wu, L.-K., Hu, J.-M., Zhang, J.-Q., 2012. Electrodeposition of zinc-doped silane films for corrosion protection of mild steels. Corros. Sci. 59 (Supplement C), 348–351.